ACS APPLIED NANO MATERIALS

www.acsanm.org

Article

Molecular Dynamics Modeling of Interfacial Interactions between Flattened Carbon Nanotubes and Amorphous Carbon: Implications for Ultra-Lightweight Composites

Prashik S. Gaikwad, Margaret Kowalik, Benjamin D. Jensen, Adri van Duin, and Gregory M. Odegard*

Cite This: *ACS Appl. Nano Mater.* 2022, 5, 5915−5924

Read Online

ACCESS | Metrics & More | Article Recommendations | Supporting Information

ABSTRACT: Flattened carbon nanotubes (flCNTs) naturally form in many carbon nanotube-based materials and can exhibit mechanical properties similar to round carbon nanotubes but with tighter packing and alignment. To facilitate the design, fabrication, and testing of flCNT-based composites for aerospace structures, computational modeling can be used to efficiently and accurately predict their performance as a function of processing parameters, such as reinforcement/matrix cross-linking. In this study, molecular dynamics modeling is used to predict the load transfer characteristics of the interface region between the flat region of flCNTs (i.e., bi-layer graphene) and amorphous carbon (AC) with various levels and locations of covalent bond cross-linking and AC mass density. The results of this study show that increasing the mass density of AC at the interface improves the load transfer capability of the interface. However, a much larger improvement is observed when cross-linking is added both to the flCNT−AC interface and between the flCNT sheets. With both types of cross-linking, substantial improvements in interfacial shear strength, transverse tension strength, and transverse tension toughness are predicted. The results of this study are important for optimizing the processing of flCNT/AC composites for demanding engineering applications.

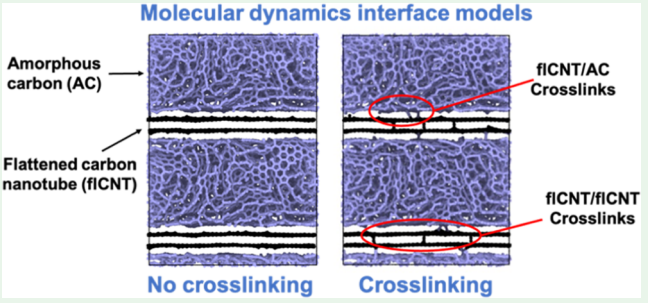

KEYWORDS: *interface/interphase, computational simulation, amorphous carbon, nano composites, polymer−matrix composites (PMCs)*

1. INTRODUCTION

There is increasing demand for new lightweight high-performance structural materials in the aerospace industry for more efficient and affordable human space travel. Due to the plateau in the advancement of traditional carbon fiber composite properties, focus has shifted to new forms of composite materials. Carbon nanotube (CNT) reinforcement, with its exceptional specific strength and stiffness, is a promising candidate for the next generation of lighter and stronger composites.[1−3] While one challenge with CNT reinforcement in composites is the difficulty in achieving sufficient levels of CNT/matrix interfacial load transfer,[4−6] a bigger challenge is the load transfer mechanisms within CNT fibers that limit composite properties.[7]

A novel resin-assisted stretching method for CNT sheets was developed by Downes et al.,[8] resulting in self-assembled, aligned, and efficiently packed flattened CNTs (flCNTs). Despite the increase in the flCNT alignment due to the stretching of CNTs, TEM-observed fracture surfaces revealed intra-stack sliding in addition to complete stack pullout. Jolowsky et al.[9] demonstrated that this fabrication method is easily scalable to macroscale composite panels, resulting in excellent flCNT/polymer load transfer and overall composite properties.

Following this pioneering work on flCNT/polymer composites, molecular dynamics (MD) simulation studies were performed on various high-performance polymer/flCNT composite models.[10−12] Patil et al.[10] investigated the interaction and load transfer characteristics of two polyimide/flCNT interfaces. Similar polymer/flCNT interface studies were performed by Pisani et al.[11] for PEEK and cyanate ester resins and by Deshpande et al.[12] for epoxy, bismaleimide, and polybenzoxazine resins. These MD studies showed that different chemical groups in the polymer had a significant effect on the polymer/flCNT interfacial interaction.

Several experimental and modeling studies have shown that these flCNT sheets form dumbbell-shaped end lobes[8,13−16] and assume a conformation similar to that of bi-layer graphene (BLG) with connected edges.[14,17,18] A density functional theory (DFT) study by Hu et al.[19] showed that end lobes exhibit reactivity and flexoelectricity. In this study, the end lobes are excluded as these features can be better captured with larger length scale models,[10] and just the BLG portion of the flCNTs is directly modeled.

Received: March 23, 2022
Accepted: April 1, 2022
Published: April 13, 2022

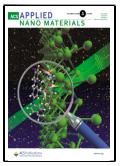

https://doi.org/10.1021/acsanm.2c01280
ACS Appl. Nano Mater. 2022, 5, 5915−5924

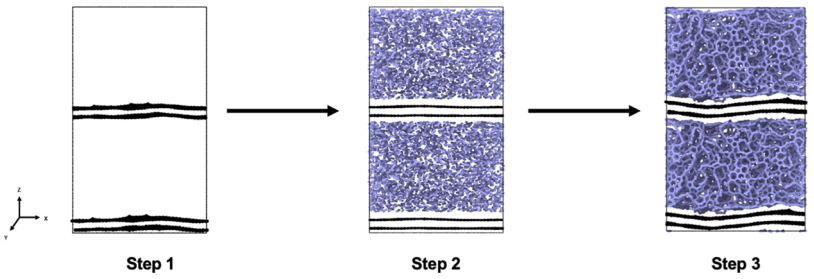

Figure 1. Molecular modeling steps for building the BLG/AC composite model: step 1—replicating BLG in the *z*-direction, step 2—inserting random carbon atoms between BLG sheets, and step 3—annealing and equilibrating the model.

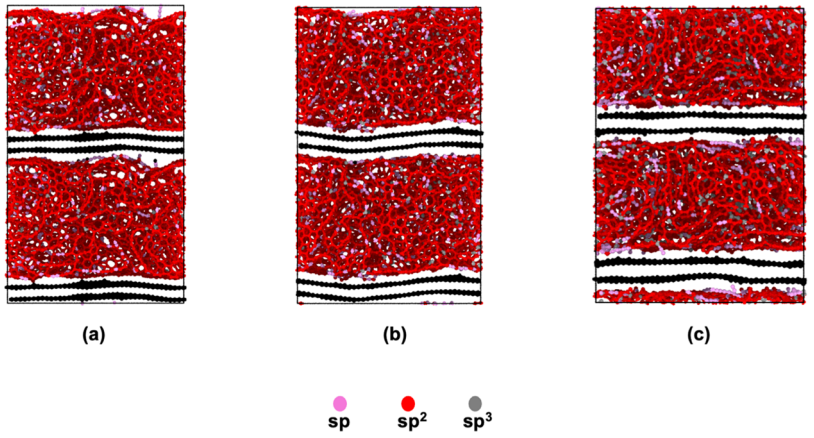

Figure 2. (a) Model 1: $\rho_{(Comp)}$ = 1.90 g/cm^3 and sp^3/sp^2 ratio of AC ~0.028, (b) model 2: $\rho_{(Comp)}$ = 1.98 g/cm^3 and sp^3/sp^2 ratio of AC ~0.035, and (c) model 3: $\rho_{(Comp)}$ = 2.25 g/cm^3 and sp^3/sp^2 ratio of AC ~0.089. The atoms are colored according to the carbon bond hybridization.

BLGs and multi-layer graphene sheets have been extensively studied using computational modeling techniques.[20−29] Muniz et al.[30] studied the mechanical behavior of interlayer bonded BLG (IB-BLG) under uniaxial tensile deformation. Chen et al.[31] comprehensively investigated the formation of all possible classes of interlayer-bonded twisted BLG structures and then subjected them to uniaxial tensile deformation. Zhang et al.[32] studied the effects of sp^3 interlayer bonding on the mechanical properties of BLG.

Previous computational and experimental studies have investigated amorphous carbon (AC) as a matrix material, particularly in composite thin films.[33−38] Jensen et al.[39] studied the mechanical properties of various continuous CNT/AC composite models. Jensen et al.[40] also studied the elastic and failure properties of discontinuous CNT/AC composites. Despite all this research on AC composites and flCNT/polymer composites, it is not known how AC interacts with the BLG region of flCNT interfaces, which is important because AC is often found in flCNT-based materials (e.g., CNT yarns) as a byproduct of the synthesis process.[41,42] Recently, Kim et al.[7] have demonstrated that CNT fibers (composed largely of flCNTs and AC) suffer from poor internal load transfer mechanisms, which adversely affects the corresponding composite strength properties. Therefore, a physical understanding of BLG/AC interfaces is needed for the development of CNT-based composite materials.

The objective of this research is to study the effect of the AC mass density $\rho_{(AC)}$ and chemical cross-linking on the interfacial characteristics of BLG/AC composites using MD simulation. To achieve this, a series of MD models of the BLG/AC interface are constructed where AC mass density, as well as the number and location of chemical cross-links between BLG and in the BLG/AC interface are varied. For each combination of mass density and cross-linking, the interfacial interaction energy (IE), shear strength, and transverse strength are predicted. It is important to note that similar to Patil et al.,[10] Pisani et al.,[11] and Deshpande at al.,[12] experimental validation of the simulated results is not performed because the relevant interfacial characterization methods for this material have not yet been developed and performed. However, to evaluate the accuracy and performance of the reactive force field parameterization used for this study, predictions of sp^3 content and Young's modulus of pure AC structure are presented and compared with experimental data in Section S1.

2. MOLECULAR MODELING

The LAMMPS software package[43] was used to perform the MD simulations in this study, and the reactive force field ReaxFF[44] with the C/H/O/N parameterization of Kowalik et al.[45] was utilized. All the atomistic visualizations were created using the OVITO software package.[46] ReaxFF is a bond-order force field and has been developed to directly simulate chemical changes such as bond scission and formation during MD simulation.[44] The accuracy of the results produced by ReaxFF for specific materials and conditions is highly dependent on the training of the parameterization used. The parametrization used herein[45] was originally developed to investigate the chemical reaction processes during the carbonization of oxidized polyacrylonitrile and poly(*p*-phenylene-2,6-benzobisoxazole) and incorporates parameters developed by Srinivasan et al.[47] (which was specifically developed for predicting accurate mechanical properties of carbon systems) and Ashraf and van Duin.[48] The former parameter set was trained for the reasonable estimation

https://doi.org/10.1021/acsanm.2c01280
ACS Appl. Nano Mater. 2022, 5, 5915−5924

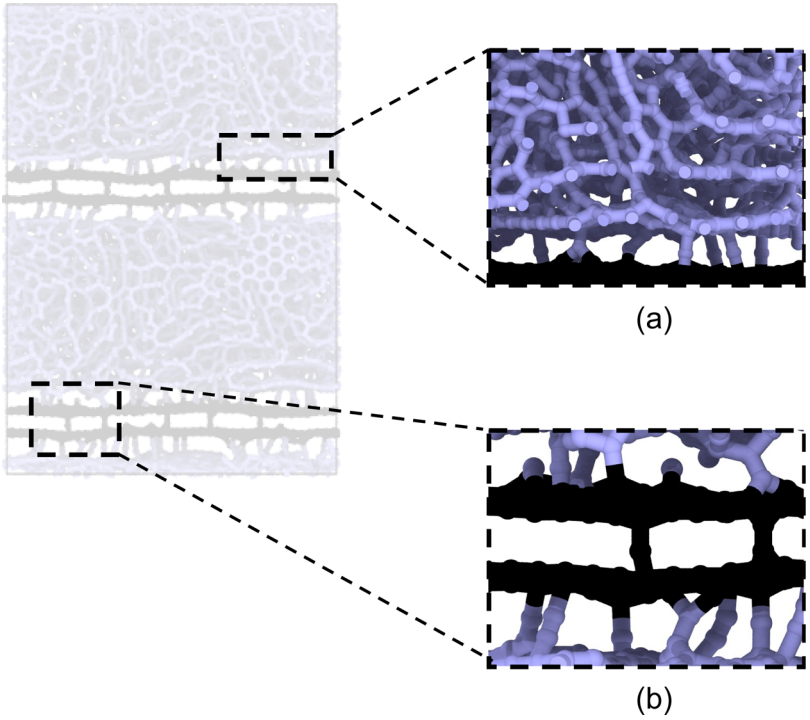

Figure 3. Two types of cross-linking: (a) BLG−AC cross-links between AC and BLG and (b) IB-BLG cross-links between BLG layers.

of graphene mechanical properties, while the latter was suitable for the production of small molecules, such as carbon dioxide, carbon monoxide, and water. The same ReaxFF parameter set was successfully applied in simulating the carbon ring network evolution for various carbonization temperatures, heating rates, and graphene concentrations.[49−51]

2.1. BLG Sheets. The "lattice" command in LAMMPS was used to create the models of the graphene sheets. The lattice parameters for the planar structure of graphene were taken from Gray et al.[52] The *x*- and *y*-dimensions of the graphene sheet were set to 50 and 25 Å, respectively. The total number of atoms were 1920, with 960 atoms per BLG sheet.

2.2. Composite Interface. The three-step procedure for building the BLG/AC interface models (Figure 1) is as follows:

1. The BLG sheet was replicated in the *z*-direction.
2. A total of 8000 carbon atoms were randomly placed in between the two sets of BLG sheets, with the initial BLG/AC composite densities of 2.12, 2.30, and 2.69 g/cm^3.
3. The randomly placed carbon atoms were heated from 300 to 3000 K at a heating rate of 200 K/ps. The temperature was held at 3000 K for 200 ps, followed by a ramp-down from 3000 to 300 K at a cooling rate of 200 K/ps. For this annealing procedure, the fixed pressure and fixed temperature (NPT) ensemble was used with an applied pressure of 1 atm and a timestep of 0.1 fs. The BLG/AC composite structures were equilibrated at room temperature and 1 atm pressure for 200 ps using the NPT ensemble with a timestep of 1 fs.

After equilibration, the final densities of the composite models were 1.90, 1.98, and 2.25 g/cm^3. Figure 2 shows the equilibrated BLG/AC composite models with different mass densities and sp^3/sp^2 ratios. The information of the total mass density $\rho_{(Comp)}$; AC mass density $\rho_{(AC)}$; sp, sp^2, and sp^3 content; and the sp^3/sp^2 ratio of the AC for the three composite models are included in Table S2. A total of three independent systems were established for each $\rho_{(Comp)}$ model to account for statistical deviations in the predicted properties.

2.3. Cross-Linking. After the equilibration simulations described in the previous section, initial cross-link sites were randomly chosen from a list of candidate BLG atoms and an AC atom was placed within the bonding distance, effectively creating a covalent bond between the BLG and AC (Figure 3a). The model was equilibrated using the NPT ensemble for 200 ps at room temperature (300 K) and pressure (1 atm). Cross-linking of this type (between the interface of the flCNT and AC) is henceforth referred to as BLG−AC cross-linking. For each of the three interface models with different mass densities, four BLG−AC cross-link models having 0, 1, 3, and 5% cross-linking densities were created. The cross-linking density is defined as the ratio of the number of BLG atoms bonded to the AC to the total number of BLG atoms. After the BLG−AC cross-linking equilibration step, new cross-links were introduced in between the BLG sheets (Figure 3b), henceforth referred to as IB-BLG cross-links. For each of the three mass densities, models having 1, 3, and 5 IB-BLG per BLG were created. Table S3 provides the details of the two types of cross-linking.

2.4. Interfacial Interaction Energy. The interfacial IE was calculated to determine the relative interaction of the AC/flCNT interface with the AC placed vertically above the flCNT sheets. The IE was calculated by subtracting the potential energies of BLG (PE_{BLG}) and AC (PE_{AC}) from the entire composite model ($PE_{Composite\ model}$)[53]

$$IE = PE_{Composite\ model} - PE_{BLG} - PE_{AC} \quad (1)$$

Greater negative values of IE indicate better interactions between BLG and AC. The procedure used is similar to those used for predicting the interaction energies of flCNT/polymer interfaces.[10−12] The models were simulated for 500 ps at 300 K and 1 atm in the NPT ensemble; thus, the simulations were non-adiabatic. The IE was computed for each replicate for each mass density and cross-linking density.

https://doi.org/10.1021/acsanm.2c01280
ACS Appl. Nano Mater. 2022, 5, 5915−5924

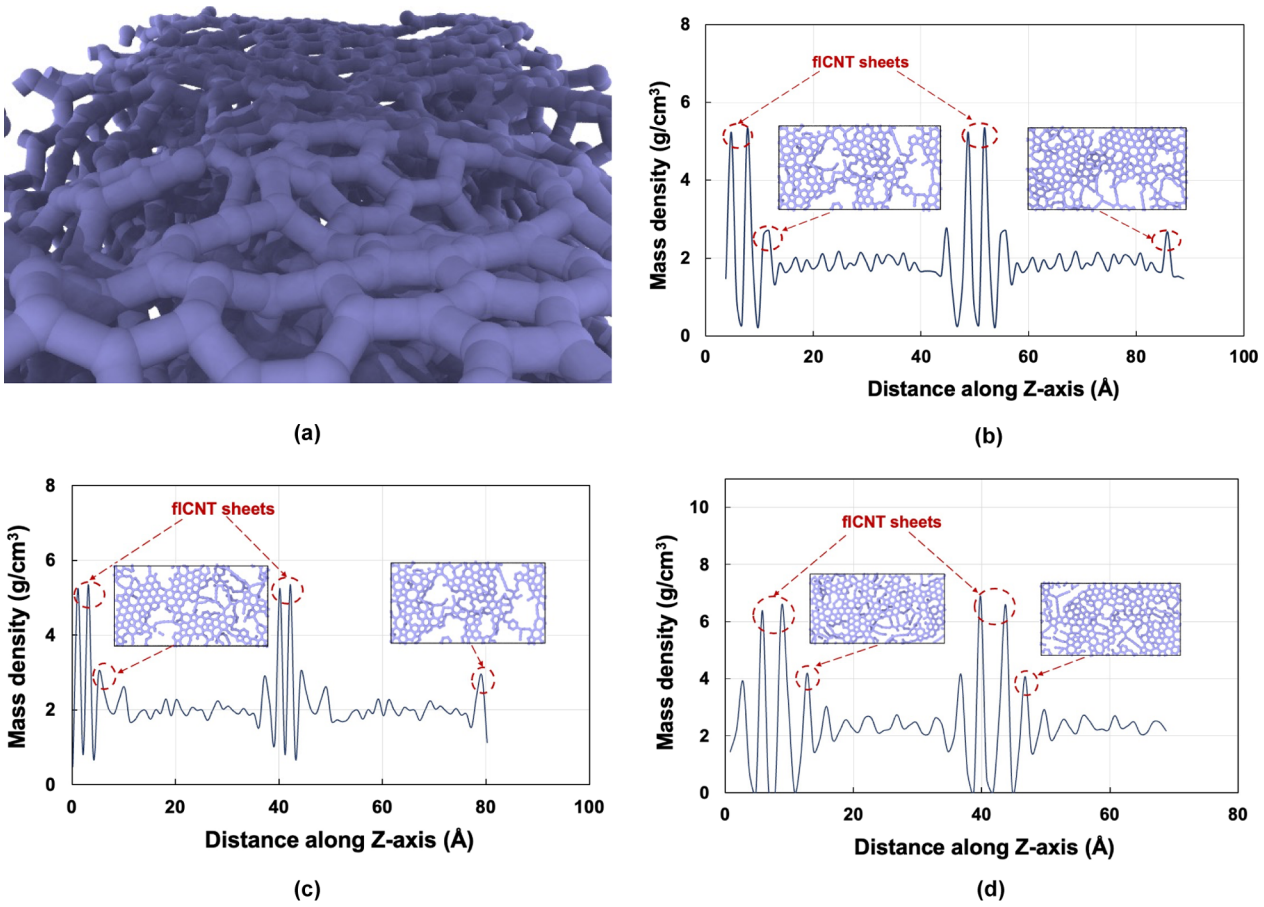

Figure 4. (a) Templating of AC near the interface region. The carbon atoms of BLG sheets are removed for visual clarity, (b) mass density profile along the *z*-axis for $\rho_{(Comp)}$ = 1.90 g/cm^3, (c) mass density profile along the *z*-axis for $\rho_{(Comp)}$ = 1.98 g/cm^3, and (d) mass density profile along the *z*-axis for $\rho_{(Comp)}$ = 2.25 g/cm^3.

2.5. Interfacial Shear Force. Pull-through MD simulations are commonly used to study the reinforcement/matrix interfacial shear strength in composites.[54−57] These simulations were performed on each replicate for every combination of mass density and cross-linking density to investigate the interfacial shear strength between the BLG and AC. Using periodic boundary conditions, the simulation process involved holding the movement of the AC at its center of mass by a spring attached to a fixed point. The "fix spring" LAMMPS command was used to create the spring with a stiffness of 1000 kcal/mol Å/Å. A pulling force was applied on each carbon atom of the two BLG using the "fix addforce" LAMMPS command. This pulling force was incrementally increased every 0.1 fs with a magnitude of 2×10^{-6} kcal/mol Å. The pull-out simulations were carried out at 300 K and 1 atm using the NPT ensemble for 500 ps.

2.6. Transverse Strength. To predict the transverse strength of the BLG/AC interfaces with BLG−AC and IB-BLG cross-links, the interface MD models were deformed uniaxially in tension along the *z*-axis, which is the direction normal to the BLG surfaces. The procedure used is similar to those used for predicting the transverse strength of flCNT/polymer interfaces.[10−12] The simulation box was deformed at a strain rate of 2×10^8 s^{-1}. The simulations were performed at 300 K and 1 atm in the NPT ensemble. For the BLG−AC cross-link models, the total strain applied was 15%. For IB-BLG cross-links, the applied strain was 15, 20, and 30% for 1, 3, and 5 covalent bonds between graphene sheets, respectively, to fully capture the failure of the BLG/AC interface. The stress−strain responses along the *z*-direction were recorded over the entire strain range. The stiffness was determined from the slope of the stress/strain response in the initial linear region. The ultimate strength was determined from the maximum stress value achieved during the simulation. The toughness was calculated from the total area under the stress−strain curve. The stiffness, ultimate strength, and toughness values were calculated in specific units GPa/g/cm^3, MPa/g/cm^3, and MJ/m^3/g/cm^3, respectively.

3. RESULTS

This section is divided into four subsections. Interfacial templating, interfacial IE, interfacial shear strength, and transverse tension results for the three composite BLG/AC models are discussed in the first, second, third, and fourth subsections, respectively.

3.1. Interfacial Templating. Figure 4a shows a representative image of the interfacial restructuring (henceforth referred to as templating) of AC in the interface region. The templating of AC occurred during the annealing and equilibration simulation steps. To further investigate the templating near the interface region, the mass density of the simulation box is plotted along the *z*-axis in Figure 4b−d for the models having mass densities of 1.90, 1.98, and 2.25 g/cm^3, respectively. The large spikes correspond to the BLG sheets, and the adjacent small peaks confirm the templating effect of AC in the interfacial region. The figure also includes snapshots of the molecular structure in the

https://doi.org/10.1021/acsanm.2c01280
ACS Appl. Nano Mater. 2022, 5, 5915−5924

templated regions to qualitatively see the alignment of aromatic carbon groups.

The interfacial templating region comprises a mixture of 3-, 4-, 5-, 6-, and 7-membered rings. The ring analysis near the interfacial region is included in Figure S4. The system with $\rho_{(Comp)}$ = 2.25 g/cm^3 shows the maximum number of 3/4/5/6/7-membered rings formed in the interface region followed by the models having $\rho_{(Comp)}$ = 1.98 g/cm^3 and $\rho_{(Comp)}$ = 1.90 g/cm^3. This implies that the degree of templating increases with the increase in the mass density of the composite model.

3.2. Interfacial Interaction Energy. The IE of the three BLG/AC composite models as a function of the BLG−AC cross-link percentage is shown in Figure 5 and reported in Table S4. The model with the highest mass density ($\rho_{(Comp)}$ = 2.25 g/cm^3) exhibits the highest level of IE followed by the composite models having $\rho_{(Comp)}$ = 1.98 g/cm^3 and $\rho_{(Comp)}$ = 1.90 g/cm^3. For the 0% BLG−AC cross-links models, the IE of $\rho_{(Comp)}$ = 2.25 g/cm^3 surpasses the IE of $\rho_{(Comp)}$ = 1.90 g/cm^3 and $\rho_{(Comp)}$ = 1.98 g/cm^3 by 615 and 570%, respectively. Thus, higher degrees of AC templating result in higher levels of interfacial interaction. With the introduction of cross-links in the interface region (1, 3, and 5% BLG−AC cross-links), a slight increase in the IE is observed. This result is consistent with modeling results by Al Mahmud et al.[58] for graphene nanoplatelet/epoxy interfaces.

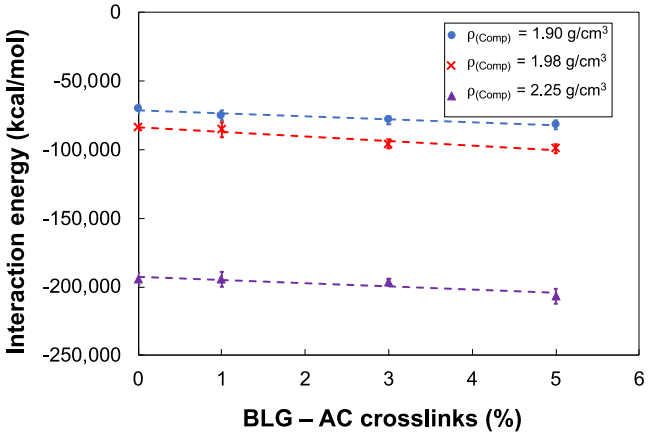

Figure 5. IE as a function of BLG−AC cross-links for the three composite models. The IE is averaged over three MD replicates, and the vertical error bar represents standard error. Trendlines are fitted to each set of data to see the trends more clearly among the scatter.

3.3. Interfacial Shear Force. Figure 6a shows a representative plot of BLG displacement versus pulling force applied on the BLG atoms with and without the addition of BLG−AC cross-links. The displacement response is divided into three regions: initial sticking, slipping onset, and smooth sliding. During initial sticking, the covalent bonds and the long-range van der Waals forces between the BLG and AC atoms are stronger than the applied pull-out force, resulting in resistance to BLG pull-out. The point at which the pull-out force is greater than the resistance from the cross-links is the onset of slipping. The breaking of the cross-links is observed at the point of slipping onset, and all of the cross-links break simultaneously (Figure 6b). After the cross-links are broken, little resistance to the pull-out of the BLGs is observed in the smooth sliding region. The inset of Figure 6a shows the BLG displacement versus the pulling force applied on each BLG atom for the 0% BLG−AC cross-link composite models. Similar behavior was observed in these systems, except that the onset of sliding was much lower, because only van der Waals forces needed to be overcome. The predicted pull-out forces for each composite model with varying amounts of BLG−AC cross-links are included in Table S5.

3.4. Transverse Strength. Figure 7 shows representative stress−strain curves for transverse tension simulations for the three un-cross-linked BLG/AC composite models. Among the un-cross-linked models, the composite model having $\rho_{(Comp)}$ = 2.25 g/cm^3 exhibits the highest transverse stiffness, ultimate strength, and toughness values. This can be attributed to the high degree of templating of AC in the interface region. The specific stiffness, specific ultimate strength, and specific toughness values for the three un-cross-linked BLG/AC composite models are included in Table S6.

Snapshots of the BLG/AC model having $\rho_{(Comp)}$ = 2.25 g/cm^3 in Figure 8a show that as the composite model is strained in the transverse direction, adhesive failure is observed in the interface region between BLG and AC, which is dominated by non-bonded (van der Waals) interactions. Snapshots of the BLG AC model having $\rho_{(Comp)}$ = 2.25 g/cm^3 with BLG−AC cross-links are shown in Figure 8b. With the addition of cross-links in the interface region between the AC and BLG, failure within the BLG sheets is observed. This indicates that the addition of cross-

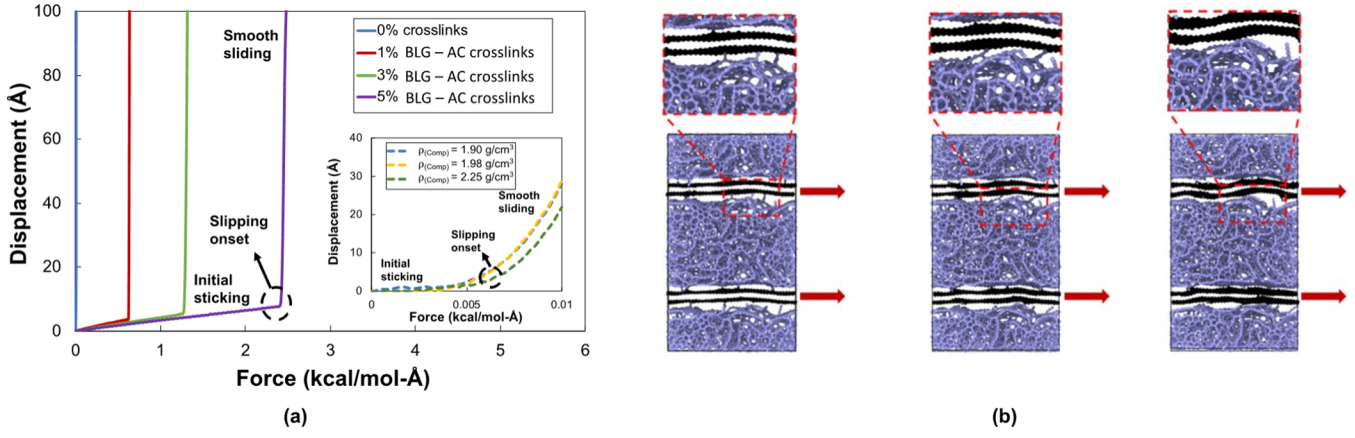

Figure 6. (a) Representative profile of BLG displacement vs the force applied on each BLG atom with BLG−AC cross-links. Representative profile of BLG displacement versus the force applied on each BLG atom for the three composite models (inset); (b) snapshots of the BLG/AC model having $\rho_{(Comp)}$ = 1.90 g/cm^3 with BLG−AC (1% cross-linking density) undergoing pull-out of BLGs.

https://doi.org/10.1021/acsanm.2c01280
ACS Appl. Nano Mater. 2022, 5, 5915−5924

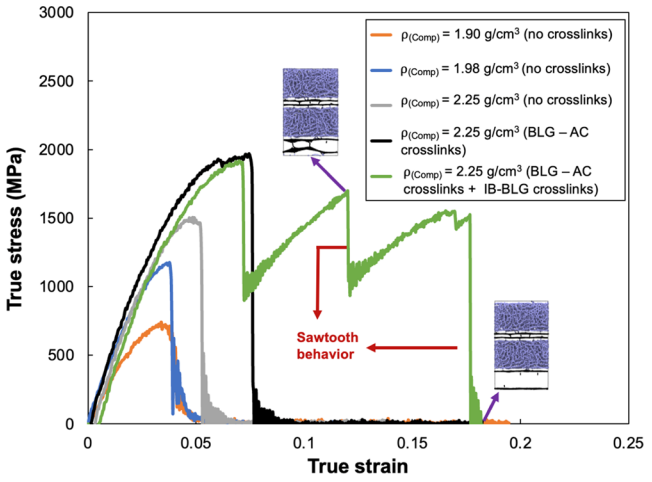

Figure 7. Representative stress–strain plots for transverse tension simulations before and after the addition of BLG–AC and IB-BLG cross-links.

links makes the interface region stronger than the region between BLG sheets, which is dominated by non-bonded van der Waals interactions. Figure 8c shows snapshots of the BLG/AC model having $\rho_{(Comp)}$ = 2.25 g/cm^3 with BLG–AC and IB-BLG cross-links. Incremental breaking of the covalent bonds between the BLG sheets was observed, which resulted in the sawtooth-type stress–strain behavior shown in Figure 7. Thus, the presence of both types of cross-links significantly increases the toughness of the interfacial region.

Figure 9a–c shows the specific stiffness, specific ultimate strength, and specific toughness, respectively, as a function of cross-linking density (BLG–AC cross-links) for the three BLG–AC composite models. With the addition of cross-links in the interface region, an increase in specific stiffness is observed (Figure 9a); however, the increase is not significant. The composite model having $\rho_{(Comp)}$ = 2.25 g/cm^3 exhibits the highest specific stiffness for all cross-linking density values. In Figure 9b, an increase in specific ultimate strength is observed for all three composite models up to a cross-linking density of 3%, after which a plateau is observed for all three systems. For specific toughness (Figure 9c), a maximum value is observed at 1% cross-linking density for all three systems. After further addition of cross-links in the interface region, a decrease in toughness is observed. This decrease is attributed to the fact that after the initial addition of cross-links (1% cross-linking density), the interface region becomes stronger than the region between

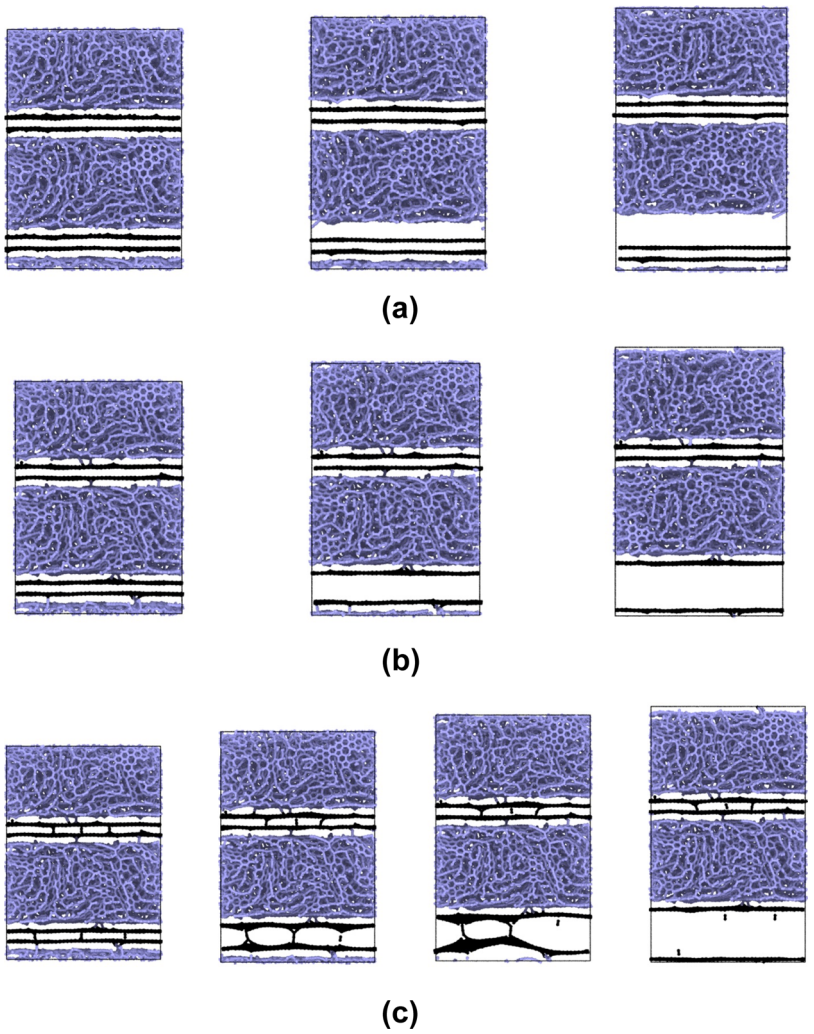

Figure 8. Snapshots of the BLG/AC model having $\rho_{(Comp)}$ = 2.25 g/cm^3 undergoing transverse deformation with: (a) no cross-links, (b) 1% BLG–AC cross-links, and (c) 1% BLG–AC and 3 IB-BLG crosslinks.

https://doi.org/10.1021/acsanm.2c01280
ACS Appl. Nano Mater. 2022, 5, 5915–5924

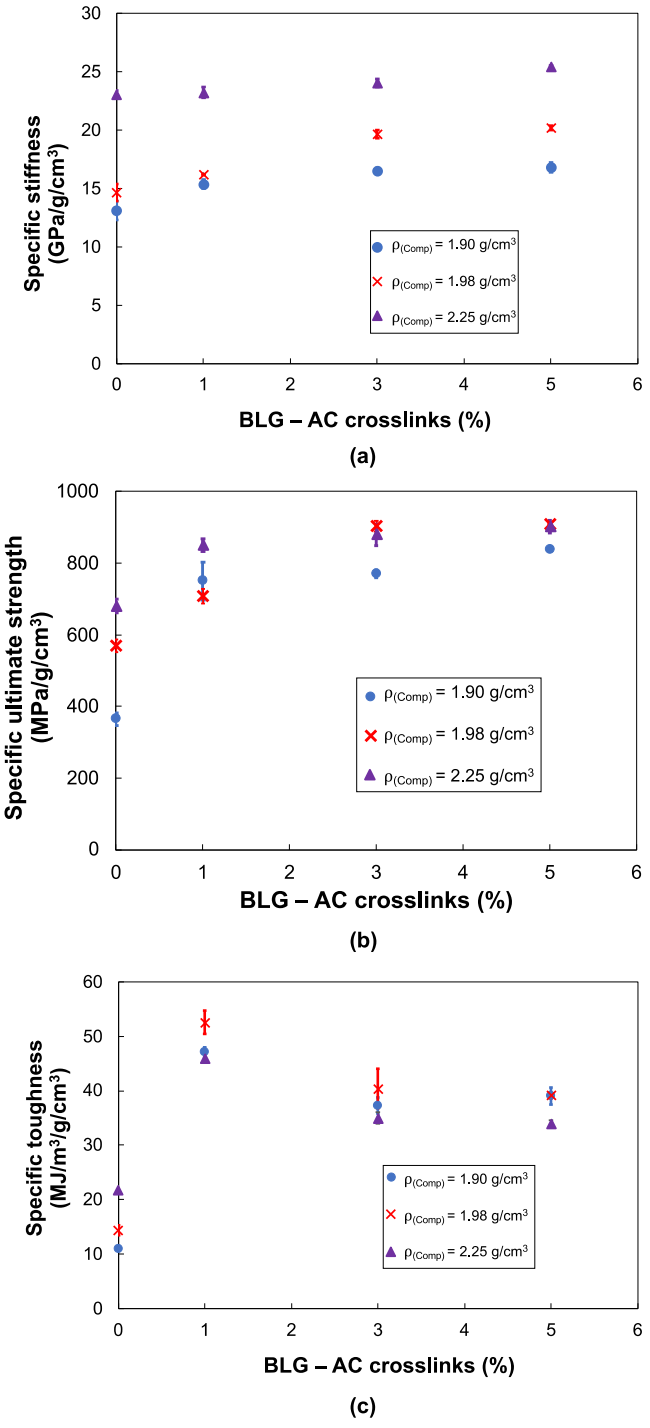

Figure 9. (a) Specific stiffness as a function of BLG−AC cross-links, (b) specific ultimate strength as a function of BLG−AC cross-links, and (c) specific toughness as a function of BLG−AC cross-links. Each data point represents the average of three MD replicates, and the vertical error bar represents standard error.

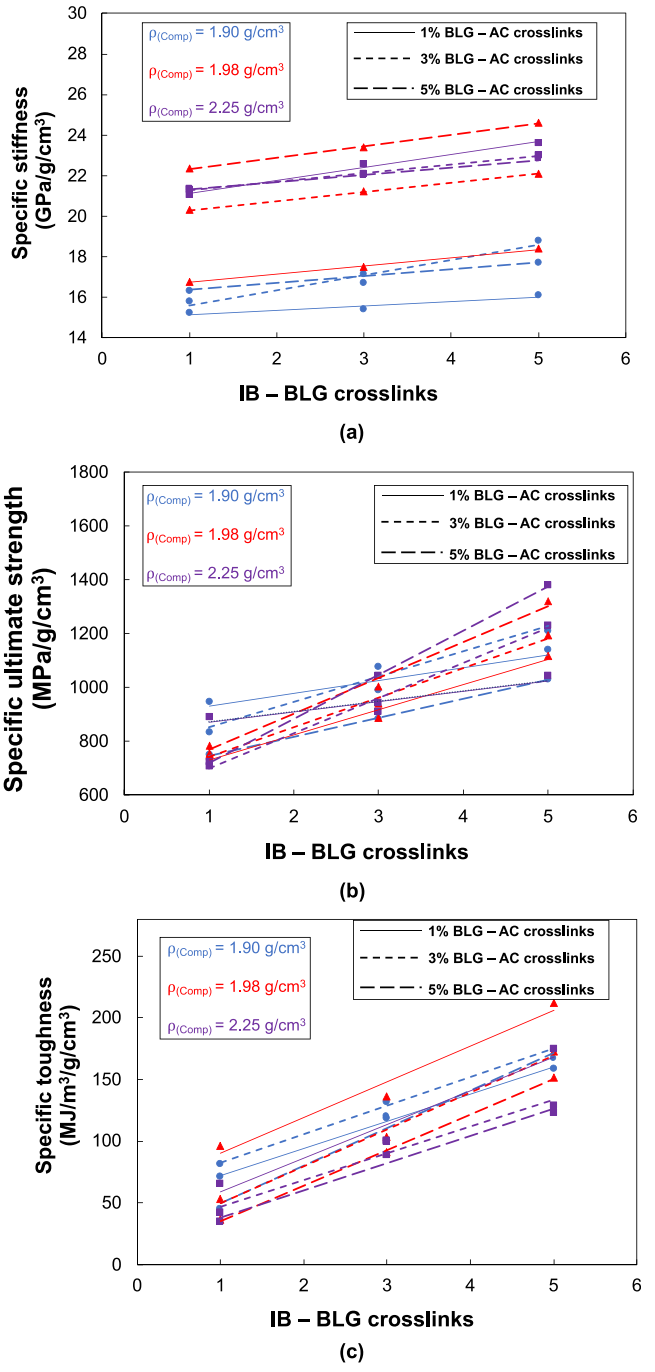

Figure 10. (a) Specific stiffness as a function of IB-BLG cross-links, (b) specific ultimate strength as a function of IB-BLG cross-links, and (c) specific toughness as a function of IB-BLG cross-links. The trendlines are fitted to each set of data to more clearly see the trends among the scatter.

BLG sheets, thus increasing the overall mechanical response of the composite system. Further addition of cross-links at the interface (>1% cross-linking density) appears to embrittle the interfacial mechanical response, likely because the higher bond density promotes simultaneous failure at multiple bond sites.

Figure 10 shows the trends of specific stiffness, specific ultimate strength, and specific toughness as a function of BLG−AC and IB-BLG cross-links for the three BLG/AC composite models. For specific stiffness (Figure 10a), an increase is observed with the increase in cross-linking density and the number of bonds within the BLG sheets. However, the increase is not significant. For the specific ultimate strength (Figure 10b), an increasing trend is observed. Depending on the composite model density and BLG−AC and IB-BLG cross-links, a 200−500 MPa increase in the specific ultimate strength is observed. For the three composite models ($\rho_{(Comp)}$ = 1.90 g/cm^3, $\rho_{(Comp)}$ = 1.98 g/cm^3, and $\rho_{(Comp)}$ = 2.25 g/cm^3), a factor of 2−4 increase in the specific toughness (Figure 10c) is observed depending on

https://doi.org/10.1021/acsanm.2c01280
ACS Appl. Nano Mater. 2022, 5, 5915−5924

the density of the composite model and BLG−AC and IB-BLG cross-links. The increase in specific toughness is attributed to the contribution from IB-BLG cross-links. During the transverse tension simulation, the breaking of the IB-BLG cross-links is observed, but the breaking of single bonds does not result in the failure of the entire composite model. The composite model is still able to sustain load due to the presence of the other cross-linking bonds, resulting in the relatively large specific toughness.

4. CONCLUSIONS

In this study, the effect of AC mass density, IB-BLG cross-linking, and BLG−AC cross-linking on the mechanical performance of BLG/AC interfaces has been determined through MD simulation. Increases in the AC mass density lead to increases in the templating in the interfacial region, which leads to increases in the interfacial IE, strength, and toughness.

Introduction of BLG−AC cross-links leads to substantial increase in the interfacial shear force of the composite. The presence of the cross-links increases the shear forces needed for the onset of slipping, as the covalent bonds transfer much higher loads than van der Waals forces alone. The introduction of BLG−AC cross-links also increases the strength and toughness of the interface when subjected to transverse tension, relative to the interface with no cross-linking. When IB-BLG cross-links are introduced to the systems that already contain BLG−AC cross-links, the transverse tensile strength and toughness significantly increase as a sawtooth-type mechanical response is observed.

The results of this study are important for optimizing the processing of flCNT/AC high-performance composites for demanding aerospace structural applications. Increasing the mass density of AC in these systems provides for the first level of improvement in interfacial properties. However, a much larger improvement in flCNT/AC load transfer comes with the addition of cross-linking, both between AC and flCNT and between adjacent flCNTs. These results indicate that moderate levels of both types of cross-linking will improve the mechanical performance of flCNT/AC composites. Too much flCNT−AC cross-linking may reduce the interfacial toughness from the optimal level.

■ ASSOCIATED CONTENT

Supporting Information

The Supporting Information is available free of charge at https://pubs.acs.org/doi/10.1021/acsanm.2c01280.

Pure AC simulation results, BLG−AC composite simulation results for mass density and carbon hybridization ratio, BLG−AC and IB-BLG cross-linking details, interfacial templating results, detailed IE predictions, interfacial shear strength results, and transverse strength predictions (PDF)

■ AUTHOR INFORMATION

Corresponding Author

Gregory M. Odegard − *Michigan Technological University, Houghton, Michigan 49931, United States;* orcid.org/0000-0001-7577-6565; Email: gmodegar@mtu.edu

Authors

Prashik S. Gaikwad − *Michigan Technological University, Houghton, Michigan 49931, United States*

Margaret Kowalik − *Pennsylvania State University, State College, Pennsylvania 16801, United States*

Benjamin D. Jensen − *NASA Langley Research Center, Hampton, Virginia 23681, United States*

Adri van Duin − *Pennsylvania State University, State College, Pennsylvania 16801, United States;* orcid.org/0000-0002-3478-4945

Complete contact information is available at: https://pubs.acs.org/10.1021/acsanm.2c01280

Notes

The authors declare no competing financial interest.

■ ACKNOWLEDGMENTS

This research was supported by NASA through the Space Technology Research Institute (STRI) for Ultra-Strong Composites by Computational Design (US-COMP), NASA grant NNX17AJ32G. SUPERIOR, a high-performance computing cluster at Michigan Technological University, was used for obtaining the MD simulation results presented in this publication.

■ REFERENCES

(1) Siochi, E. J.; Harrison, J. S. Structural nanocomposites for aerospace applications. *MRS Bull.* **2015**, *40*, 829−835.

(2) Kim, J.-W.; Sauti, G.; Cano, R. J.; Wincheski, R. A.; Ratcliffe, J. G.; Czabaj, M.; Gardner, N. W.; Siochi, E. J. Assessment of carbon nanotube yarns as reinforcement for composite overwrapped pressure vessels. *Composites, Part A* **2016**, *84*, 256−265.

(3) Singh, P. K.; Sharma, K.; Kumar, A.; Shukla, M. Effects of functionalization on the mechanical properties of multiwalled carbon nanotubes: A molecular dynamics approach. *J. Compos. Mater.* **2017**, *51*, 671−680.

(4) Zhang, X.; Li, Q.; Holesinger, T. G.; Arendt, P. N.; Huang, J.; Kirven, P. D.; Clapp, T. G.; DePaula, R. F.; Liao, X.; Zhao, Y.; Zheng, L.; Peterson, D. E.; Zhu, Y. Ultrastrong, Stiff, and Lightweight Carbon-Nanotube Fibers. *Adv. Mater.* **2007**, *19*, 4198−4201.

(5) Mora, R. J.; Vilatela, J. J.; Windle, A. H. Properties of composites of carbon nanotube fibres. *Compos. Sci. Technol.* **2009**, *69*, 1558−1563.

(6) Odegard, G. M.; Liang, R.; Wise, K. E. Special issue on carbon nanotube composites. *Compos. Sci. Technol.* **2018**, *166*, 1−2.

(7) Kim, J.-W.; Sauti, G.; Jensen, B. D.; Smith, J. G.; Wise, K. E.; Wincheski, R. A.; Cano, R. J.; Siochi, E. J. Modifying carbon nanotube fibers: A study relating apparent interfacial shear strength and failure mode. *Carbon* **2021**, *173*, 857−869.

(8) Downes, R. D.; Hao, A.; Park, J. G.; Su, Y.-F.; Liang, R.; Jensen, B. D.; Siochi, E. J.; Wise, K. E. Geometrically constrained self-assembly and crystal packing of flattened and aligned carbon nanotubes. *Carbon* **2015**, *93*, 953−966.

(9) Jolowsky, C.; Sweat, R.; Park, J. G.; Hao, A.; Liang, R. Microstructure evolution and self-assembling of CNT networks during mechanical stretching and mechanical properties of highly aligned CNT composites. *Compos. Sci. Technol.* **2018**, *166*, 125−130.

(10) Patil, S. U.; Radue, M. S.; Pisani, W. A.; Deshpande, P.; Xu, H.; Al Mahmud, H.; Dumitrică, T.; Odegard, G. M. Interfacial characteristics between flattened CNT stacks and polyimides: A molecular dynamics study. *Comput. Mater. Sci.* **2020**, *185*, 109970.

(11) Pisani, W. A.; Radue, M. S.; Patil, S. U.; Odegard, G. M. Interfacial modeling of flattened CNT composites with cyanate ester and PEEK polymers. *Composites, Part B* **2021**, *211*, 108672.

(12) Deshpande, P. P.; Radue, M. S.; Gaikwad, P.; Bamane, S.; Patil, S. U.; Pisani, W. A.; Odegard, G. M. Prediction of the Interfacial Properties of High-Performance Polymers and Flattened CNT-Reinforced Composites Using Molecular Dynamics. *Langmuir* **2021**, *37*, 11526−11534.

(13) Xu, H.; Drozdov, G.; Park, J. G.; Jensen, B. D.; Wise, K. E.; Liang, Z.; Odegard, G. M.; Siochi, E. J.; Dumitrică, T. Computationally

Guided Design of Large-Diameter Carbon Nanotube Bundles for High-Strength Materials. *ACS Appl. Nano Mater.* **2021**, *4*, 11115−11125.
(14) Del Grande, R. R.; Fonseca, A. F.; Capaz, R. B. Energy barriers for collapsing large-diameter carbon nanotubes. *Carbon* **2020**, *159*, 161−165.
(15) Torres-Dias, A. C.; Cerqueira, T. F. T.; Cui, W.; Marques, M. A. L.; Botti, S.; Machon, D.; Hartmann, M. A.; Sun, Y.; Dunstan, D. J.; San-Miguel, A. From mesoscale to nanoscale mechanics in single-wall carbon nanotubes. *Carbon* **2017**, *123*, 145−150.
(16) Elliott, J. A.; Sandler, J. K.; Windle, A. H.; Young, R. J.; Shaffer, M. S. Collapse of Single-Wall Carbon Nanotubes is Diameter Dependent. *Phys. Rev. Lett.* **2004**, *92*, 095501.
(17) Zhang, S.; Khare, R.; Belytschko, T.; Hsia, K. J.; Mielke, S. L.; Schatz, G. C. Transition states and minimum energy pathways for the collapse of carbon nanotubes. *Phys. Rev. B: Condens. Matter Mater. Phys.* **2006**, *73*, 075423.
(18) Lu, W.; Chou, T.-W.; Kim, B.-S. Radial deformation and its related energy variations of single-walled carbon nanotubes. *Phys. Rev. B: Condens. Matter Mater. Phys.* **2011**, *83*, 134113.
(19) Hu, C.; Dernov, A.; Xu, H.; Drozdov, G.; Dumitrică, T. Ab initio predictions of graphite-like phase with anomalous grain boundaries and flexoelectricity from collapsed carbon nanotubes. *J. Chem. Phys.* **2021**, *154*, 044701.
(20) Nourbakhsh, A.; Cantoro, M.; Klekachev, A. V.; Pourtois, G.; Vosch, T.; Hofkens, J.; van der Veen, M. M.; De Gendt, S.; Sels, B. F. Single Layer vs Bilayer Graphene: A Comparative Study of the Effects of Oxygen Plasma Treatment on Their Electronic and Optical Properties. *J. Phys. Chem. C* **2011**, *115*, 16619−16624.
(21) Wang, Q. H.; Shih, C.-J.; Paulus, G. L. C.; Strano, M. S. Evolution of Physical and Electronic Structures of Bilayer Graphene upon Chemical Functionalization. *J. Am. Chem. Soc.* **2013**, *135*, 18866−18875.
(22) McCann, E.; Abergel, D. S. L.; Fal'ko, V. I. Electrons in bilayer graphene. *Solid State Commun.* **2007**, *143*, 110−115.
(23) Ohta, T.; Bostwick, A.; Seyller, T.; Horn, K.; Rotenberg, E. Controlling the Electronic Structure of Bilayer Graphene. *Science* **2006**, *313*, 951−954.
(24) Castro, E. V.; Peres, N. M. R.; Santos, J. M. B. L. d.; Guinea, F.; Neto, A. H. C. Bilayer graphene: gap tunability and edge properties. *J. Phys.: Conf. Ser.* **2008**, *129*, 012002.
(25) Muniz, A. R.; Maroudas, D. Formation of fullerene superlattices by interlayer bonding in twisted bilayer graphene. *J. Appl. Phys.* **2012**, *111*, 043513.
(26) Machado, A. S.; Maroudas, D.; Muniz, A. R. Tunable mechanical properties of diamond superlattices generated by interlayer bonding in twisted bilayer graphene. *Appl. Phys. Lett.* **2013**, *103*, 013113.
(27) Muniz, A. R.; Maroudas, D. Superlattices of Fluorinated Interlayer-Bonded Domains in Twisted Bilayer Graphene. *J. Phys. Chem. C* **2013**, *117*, 7315−7325.
(28) Zhang, J.; Zhao, J. Mechanical properties of bilayer graphene with twist and grain boundaries. *J. Appl. Phys.* **2013**, *113*, 43514.
(29) Kumar, A.; Sharma, K.; Dixit, A. R. A review on the mechanical and thermal properties of graphene and graphene-based polymer nanocomposites: understanding of modelling and MD simulation. *Mol. Simul.* **2020**, *46*, 136−154.
(30) Muniz, A. R.; Machado, A. S.; Maroudas, D. Mechanical behavior of interlayer-bonded nanostructures obtained from bilayer graphene. *Carbon* **2015**, *81*, 663−677.
(31) Chen, M.; Muniz, A. R.; Maroudas, D. Formation and Mechanical Behavior of Nanocomposite Superstructures from Interlayer Bonding in Twisted Bilayer Graphene. *ACS Appl. Mater. Interfaces* **2018**, *10*, 28898−28908.
(32) Zhang, Y. Y.; Wang, C. M.; Cheng, Y.; Xiang, Y. Mechanical properties of bilayer graphene sheets coupled by sp3 bonding. *Carbon* **2011**, *49*, 4511−4517.
(33) Fyta, M. G.; Remediakis, I. N.; Kelires, P. C.; Papaconstantopoulos, D. A. Insights into the fracture mechanisms and strength of amorphous and nanocomposite carbon. *Phys. Rev. Lett.* **2006**, *96*, 185503.
(34) Fyta, M.; Mathioudakis, C.; Remediakis, I. N.; Kelires, P. C. Carbon-based nanostructured composite films: elastic, mechanical and optoelectronic properties derived from computer simulations. *Surf. Coat. Technol.* **2011**, *206*, 696−702.
(35) Mathioudakis, C.; Fyta, M. Computer simulations of nano-structured carbon under tensile load: Electronic structure and optical gap. *Diamond Relat. Mater.* **2012**, *23*, 50−53.
(36) Amaratunga, G. A. J.; Chhowalla, M.; Kiely, C. J.; Alexandrou, I.; Aharonov, R.; Devenish, R. M. Hard elastic carbon thin films from linking of carbon nanoparticles. *Nature* **1996**, *383*, 321−323.
(37) Wei, C.; Wang, C.-I.; Tai, F.-C.; Ting, K.; Chang, R.-C. The effect of CNT content on the surface and mechanical properties of CNTs doped diamond like carbon films. *Diamond Relat. Mater.* **2010**, *19*, 562−566.
(38) Schittenhelm, H.; Geohegan, D. B.; Jellison, G. E.; Puretzky, A. A.; Lance, M. J.; Britt, P. F. Synthesis and characterization of single-wall carbon nanotube−amorphous diamond thin-film composites. *Appl. Phys. Lett.* **2002**, *81*, 2097−2099.
(39) Jensen, B. D.; Wise, K. E.; Odegard, G. M. Simulation of mechanical performance limits and failure of carbon nanotube composites. *Modell. Simul. Mater. Sci. Eng.* **2016**, *24*, 025012.
(40) Jensen, B. D.; Odegard, G. M.; Kim, J.-W.; Sauti, G.; Siochi, E. J.; Wise, K. E. Simulating the effects of carbon nanotube continuity and interfacial bonding on composite strength and stiffness. *Compos. Sci. Technol.* **2018**, *166*, 10−19.
(41) Lin, Y.; Kim, J.-W.; Connell, J. W.; Lebrón-Colón, M.; Siochi, E. J. Purification of Carbon Nanotube Sheets. *Adv. Eng. Mater.* **2015**, *17*, 674−688.
(42) Pumera, M.; Ambrosi, A.; Chng, E. L. K. Impurities in graphenes and carbon nanotubes and their influence on the redox properties. *Chem. Sci.* **2012**, *3*, 3347−3355.
(43) Plimpton, S. Fast Parallel Algorithms for Short-Range Molecular Dynamics. *J. Comput. Phys.* **1995**, *117*, 1−19.
(44) van Duin, A. C. T.; Dasgupta, S.; Lorant, F.; Goddard, W. A. ReaxFF: A Reactive Force Field for Hydrocarbons. *J. Phys. Chem. A* **2001**, *105*, 9396−9409.
(45) Kowalik, M.; Ashraf, C.; Damirchi, B.; Akbarian, D.; Rajabpour, S.; van Duin, A. C. T. Atomistic Scale Analysis of the Carbonization Process for C/H/O/N-Based Polymers with the ReaxFF Reactive Force Field. *J. Phys. Chem. B* **2019**, *123*, 5357−5367.
(46) Stukowski, A. Visualization and analysis of atomistic simulation data with OVITO−the Open Visualization Tool. *Modell. Simul. Mater. Sci. Eng.* **2010**, *18*, 015012.
(47) Srinivasan, S. G.; van Duin, A. C. T.; Ganesh, P. Development of a ReaxFF Potential for Carbon Condensed Phases and Its Application to the Thermal Fragmentation of a Large Fullerene. *J. Phys. Chem. A* **2015**, *119*, 571−580.
(48) Ashraf, C.; van Duin, A. C. T. Extension of the ReaxFF Combustion Force Field toward Syngas Combustion and Initial Oxidation Kinetics. *J. Phys. Chem. A* **2017**, *121*, 1051−1068.
(49) Zhang, L.; Kowalik, M.; Gao, Z.; Ashraf, C. M.; Rajabpour, S.; Bumgardner, C.; Schwab, Y.; Damirchi, B.; Zhu, J.; Akbarian, D.; Klett, J. W.; van Duin, A. C. T.; Li, X. Converting PBO fibers into carbon fibers by ultrafast carbonization. *Carbon* **2020**, *159*, 432−442.
(50) Rajabpour, S.; Mao, Q.; Gao, Z.; Khajeh Talkhoncheh, M.; Zhu, J.; Schwab, Y.; Kowalik, M.; Li, X.; van Duin, A. C. T. Low-temperature carbonization of polyacrylonitrile/graphene carbon fibers: A combined ReaxFF molecular dynamics and experimental study. *Carbon* **2021**, *174*, 345−356.
(51) Gao, Z.; Zhu, J.; Rajabpour, S.; Joshi, K.; Kowalik, M.; Croom, B.; Schwab, Y.; Zhang, L.; Bumgardner, C.; Brown, K. R.; Burden, D.; Klett, J. W.; van Duin, A. C. T.; Zhigilei, L. V.; Li, X. Graphene reinforced carbon fibers. *Sci. Adv.* **2020**, *6*, No. eaaz4191.
(52) Gray, D.; McCaughan, A.; Mookerji, B. Crystal structure of graphite, graphene and silicon. *Phys. Solid State. Appl.* **2009**, *6*, 730−732.
(53) Radue, M. S.; Odegard, G. M. Multiscale modeling of carbon fiber/carbon nanotube/epoxy hybrid composites: Comparison of epoxy matrices. *Compos. Sci. Technol.* **2018**, *166*, 20−26.

https://doi.org/10.1021/acsanm.2c01280
ACS Appl. Nano Mater. 2022, 5, 5915−5924

(54) Li, Y.; Liu, Y.; Peng, X.; Yan, C.; Liu, S.; Hu, N. Pull-out simulations on interfacial properties of carbon nanotube-reinforced polymer nanocomposites. *Comput. Mater. Sci.* **2011**, *50*, 1854−1860.
(55) Lv, C.; Xue, Q.; Xia, D.; Ma, M. Effect of chemisorption structure on the interfacial bonding characteristics of graphene−polymer composites. *Appl. Surf. Sci.* **2012**, *258*, 2077−2082.
(56) Lv, C.; Xue, Q.; Xia, D.; Ma, M.; Xie, J.; Chen, H. Effect of Chemisorption on the Interfacial Bonding Characteristics of Graphene−Polymer Composites. *J. Phys. Chem. C* **2010**, *114*, 6588−6594.
(57) Al Mahmud, H.; Radue, M. S.; Odegard, G. M. "Molecular Dynamics Modeling to Probe the Effect of Surface Functionalization on the Interfacial Adhesion and Shear Strength of Graphene/Epoxy Nanocomposites". *ASCE Earth & Space Conference, Virtual Conference*, April 19−23, 2021.
(58) Al Mahmud, H.; Radue, M. S.; Chinkanjanarot, S.; Odegard, G. M. Multiscale Modeling of Epoxy-Based Nanocomposites Reinforced with Functionalized and Non-Functionalized Graphene Nanoplatelets. *Polymers* **2021**, *13*, 1958.

https://doi.org/10.1021/acsanm.2c01280
ACS Appl. Nano Mater. 2022, 5, 5915−5924